Electronic Supplementary Information

CO$_2$ generated amorphous metal organic frameworks for efficient CO$_2$ conversion

Zhou Fang,[a,b] Yue Hu,[a,b] Bing Yao,[a,b] Zhizhen Ye,[a,b] Xinsheng Peng [a,b,]*

[a]State Key Laboratory of Silicon and Advanced Semiconductor Materials, School of Materials Science and Engineering, Zhejiang University, Hangzhou 310027, P. R. China.

[b]Wenzhou Key Laboratory of Novel Optoelectronic and Nanomaterials, Institute of Wenzhou, Zhejiang University, Wenzhou 325006, Zhejiang, P. R. China.

[a,b,*] Email: pengxinsheng@zju.edu.cn

Experimental section

Materials

All chemicals and solvents used were of reagent grade and used without any further purification. Copper nitrate ($Cu(NO_3)_2$, cobalt acetate ($Co(OAc)_2$, N,N'-dimethylformamide (DMF), nickel nitrate ($Ni(NO_3)_2$), zinc acetate ($Zn(OAc)_2$), iso-propanol (^iPrOH), terephthalic acid and 1,8-Diazabicyclo [5.4.0]undec-7-ene (DBU, $C_9H_{16}N_2$ 99%), were purchased from Shanghai Macklin Biochemical Technology Co., Ltd. Silver nitrate ($AgNO_3$) was purchased from Sinopharm Chemical Reagent Co. Ltd. Anhydrous methanol (CH_3OH, AR), anhydrous ethanol (C_2H_5OH, AR), and toluene (C_7H_8, AR) were brought from Chengdu Kelong Chemical Reagent Co., Ltd. Tetrabutylammonium bromide (TBAB, $C_{16}H_{36}BrN$, 99%, AR), styrene oxide (SO, C_8H_8O98%) and sodium sulfate (Na_2SO_4, AR) were provided by Shanghai Macklin Biochemical Technology Co., Ltd. The ultrapure water of 18.2 MΩ used throughout the experiments was produced by a Millipore direct-Q system (Millipore). CO_2 and Ar gases were brought from Minxing Chemical Technology Co., Ltd. with purity of 99.999%.

Synthesis of Cu_xPDC

Firstly, $Cu(NO_3)_2 \cdot xH_2O$ powders were dissolved in 10 mL DMF and the powders of H_2PZ were dispersed in 10 mL ^iPrOH in two Schlenk tubes with a rubber septum, respectively. Then, the tube equipped with H_2PZ solution was sealed and injected with DBU under the Ar atmosphere. The resultant transparent solution was stirred for 3 min. Subsequently, two Schlenk tubes were connected with double-row tubes and purged with CO_2 three times to displace the reaction environment. Soon afterwards, the $Cu(NO_3)_2$ solution was injected into the H_2PZ solution without contact with air with assistance of double-ended needles, and the precipitate was formed immediately. The reaction mixture was continuously stirred under CO_2 flowing overnight to complete the reaction. After that, the precipitate was collected by filtration and washed with DMF, ^iPrOH and anhydrous methanol, and dried under vacuum at 50 ℃. All the washing solvents were purged with Ar gases to remove moisture and oxygen. Cu_xPDC (x represents the molar ratio of copper nitrate to piperazine, normalized 1 for piperazine segments) MOF prepared by different ratios of metal salts and piperazine ligands.

Synthesis of Cu_xBDC

$Cu(NO_3)_2 \cdot xH_2O$ and terephthalic acid were dissolved in DMF solvent in turn, then, hydrothermal reactor was placed in oven at 110 ℃ for 6 h. Cu_xBDC (x represents the molar ratio of copper nitrate to terephthalic acid, normalized 1 for terephthalic acid segments) MOF prepared by different ratios of metal salts under identical conditions.

Synthesis of $Cu_1PDC-Dn$

The major procedure of $Cu_1PDC-Dn$ MOFs preparation was identical to the synthesis of

Cu_xPDC. In order to control the other synthesized conditions, the ratio of metal salts and piperazine ligands was kept as 1 (Cu_1PDC MOF). Subsequently, a series of Cu_1PDC-Dn MOFs (n represents the molar ratio of piperazine to DBU) were fabricated while adding various DBU modulators during the synthesis.

Synthesis of Cu_1PDC-D_4 with different amounts of acidic modulator (HCl)

The pH-responsive of DBU was considered to be a possible reason for the crystallinity adjustment of CuPDC MOF. To illustrate the influence on pH value, the amounts of metal salts, H_2PZ and DBU were maintained in the preparation process, moreover, introduced acidic modulator HCl in this system to adjust the pH value of the reaction solution.

Synthesis of Co_xPDC

The synthesized process of Co_xPDC was similar to Cu_xPDC. $Co(OAc)_2 \cdot xH_2O$ powders were dissolved in 10 mL DMF and H_2PZ were dispersed in 10 mL ^iPrOH. Then, DBU was injected into H_2PZ solution under the Ar atmosphere. Subsequently, the $Co(OAc)_2$ solution was injected into the H_2PZ solution without contact with air, and the precipitate was formed immediately. The reaction mixture was continuously stirred under CO_2 flowing overnight to complete the reaction. After that, the precipitate was collected by filtration and washed with DMF, ^iPrOH and anhydrous methanol, and dried under vacuum at 50 °C. All the washing solvents were purged with Ar gases to remove moisture and oxygen. Co_xPDC (x represents the molar ratio of cobalt salts to piperazine, normalized 1 for piperazine segments) MOF prepared by different ratios of metal salts and piperazine ligands.

Synthesis of Co_xBDC

$Co(OAc)_2 \cdot xH_2O$ and terephthalic acid were dissolved in DMF solvent in turn, then, hydrothermal reactor was placed in oven at 110 °C for 6 h. Co_xBDC (x represents the molar ratio of cobalt acetate to terephthalic acid, normalized 1 for terephthalic acid segments) MOF prepared by different ratios of metal salts under identical conditions.

Synthesis of Ni_xPDC

The synthesized process of Ni_xPDC was similar to Cu_xPDC. $Ni(NO_3)_2 \cdot xH_2O$ powders were dissolved in 10 mL DMF and H_2PZ were dispersed in 10 mL ^iPrOH. Then, DBU was injected into H_2PZ solution under the Ar atmosphere. Subsequently, the $Ni(NO_3)_2$ solution was injected into the H_2PZ solution without contact with air, and the precipitate was formed immediately. The reaction mixture was continuously stirred under CO_2 flowing overnight to complete the reaction. After that, the precipitate was collected by filtration and washed with DMF, ^iPrOH and anhydrous methanol, and dried under vacuum at 50 °C. All the washing solvents were purged with Ar gases to remove moisture and oxygen. Ni_xPDC (x represents the molar ratio of cobalt salts to piperazine, normalized 1 for piperazine segments) MOF prepared by different ratios of metal salts and piperazine ligands.

Synthesis of Ag_xPDC

The synthesized process of Ag_xPDC was similar to Cu_xPDC. $AgNO_3$ powders were dissolved in 10 mL DMF and H_2PZ were dispersed in 10 mL ^iPrOH. Then, DBU was injected into H_2PZ

solution under the Ar atmosphere. Subsequently, the Ni(NO$_3$)$_2$ solution was injected into the H$_2$PZ solution without contact with air, and the precipitate was formed immediately. The reaction mixture was continuously stirred under CO$_2$ flowing overnight to complete the reaction. All the solutions need to be placed in the darkness to prevent decomposition of AgNO$_3$. After that, the precipitate was collected by filtration and washed with DMF, ^{i}PrOH and anhydrous methanol, and dried under vacuum at 50 °C. All the washing solvents were purged with Ar gases to remove moisture and oxygen. Ag$_x$PDC (x represents the molar ratio of cobalt salts to piperazine, normalized 1 for piperazine segments) MOF prepared by different ratios of metal salts and piperazine ligands.

Synthesis of Zn$_x$PDC

The synthesized process of Zn$_x$PDC was similar to Cu$_x$PDC. Zn(OAc)$_2$·xH$_2$O powders were dissolved in 10 mL DMF and H$_2$PZ were dispersed in 10 mL ^{i}PrOH. Then, DBU was injected into H$_2$PZ solution under the Ar atmosphere. Subsequently, the Ni(NO$_3$)$_2$ solution was injected into the H$_2$PZ solution without contact with air, and the precipitate was formed immediately. The reaction mixture was continuously stirred under CO$_2$ flowing overnight to complete the reaction. After that, the precipitate was collected by filtration and washed with DMF, ^{i}PrOH and anhydrous methanol, and dried under vacuum at 50 °C. All the washing solvents were purged with Ar gases to remove moisture and oxygen. Zn$_x$PDC (x represents the molar ratio of cobalt salts to piperazine, normalized 1 for piperazine segments) MOF prepared by different ratios of metal salts and piperazine ligands.

Characterization

Powder X-ray diffraction measurements were performed on SmartLab Powder diffractometers (Rigaku Corporation, Japan) using Cu Kα (λ=1.5406 Å) radiation over 2θ range of 5° - 40°. The samples were kept in vacuum oven before XRD test, and after finishing the detection, the samples were sealed in a glass bottle under the Ar atmosphere. Scanning electron microscopy (SEM) and transmission electron microscopy (TEM) images were collected using Sigma 300 (Zeiss, German) and HT-7700 TEM (Hitachi, Japan), respectively, assisted with accessories of X-ray energy dispersive spectrometer (EDS) analysis. The cross-polarization magic angle spinning carbon-13 nuclear magnetic resonance (CPMAS ^{13}C NMR) measurements were conducted on Avance III HD (Bruker, German) spectrometer operating at 400 MHz. The Fourier-transform infrared spectroscopy (FTIR) spectra were recorded using a KBr pellet as background in the range of 4000 ~ 400cm^{-1} on Nicolet iS50 spectrometer (ThermoFisher, US). X-ray photoelectron spectroscopy (XPS) spectra were performed on Nexsa (ThermoFisher, US) with Al Kα X-ray source (1486.6 eV). The binding energies were calibrated using the C 1s peak at 284.8 eV as the internal standard. Thermogravimetric analysis (TGA) and differential scanning calorimeter (DSC) tests were carried out on STA-2500 analyzer (NETZSCH, German) under air atmosphere. The TGA and DSC were measured over the temperature range of 50 °C ~ 800 °C with a heating rate of 5 °C/min under the air stream. Nitrogen adsorption measurements were collected at 77 K on ASAP 2460 (Micromeritics Instrument Corporation, US). NH$_3$ temperature programmed desorption (NH$_3$-TPD) and CO$_2$ temperature programmed desorption (CO$_2$-TPD) were carried out on a TP-5080 multi-functional automatic adsorption instrument (Xianquan, China) to detect the Lewis acid sites and Lewis base sites, respectively. The signals were recorded by monitoring the desorbed gas with a TCD detector. As for

the CO_2-TPD test, 100 mg catalyst with 40 ~ 60 mesh was dehydrated with Ar gases at 353 K for 3 h and then cooled to 323 K. Under the same temperature, the powders started adsorption in a gas flow of 10 vol% CO_2/He with a flow rate of 30 mL/min, until the baseline was stable, which represented the adsorption saturation. Subsequently, the catalyst was heated from 323 K to 473 K at a rate of 5 °C/min, and the signal of CO_2 desorption was detected by TCD. And as for NH_3-TPD detection, other conditions were maintained identically while the concentration of gas flow was substituted by 5 vol% NH_3/He. To determine the ratio of metal salts and CO_2-based organic ligands, the elemental content of N and metal atoms (Cu/Co) were measured, respectively. An inductively coupled plasma optical emission spectrometer (ICP-OES) was conducted on Avio 200 (Perkin Elmer, US). The obtained powders were dissolved in aqua regia and diluted them to a suitable concentration for ICP detection. The content of N was determined by elemental analyzer EA3000 (Euro Vector, Italy).

The extended X-ray absorption fine structure (EXAFS) measurements were carried out on the samples (crystalline CuBDC, crystalline CuPDC and amorphous CuPDC) at 21A X-ray nanodiffraction beamline of Taiwan Photon Source (TPS). National Synchrotron Radiation Research Center (NSRRC). X-ray absorption fine structure (XAFS) experiments at the Cu K-edge were undertaken at the X-ray absorption (XAS) beamline. This beamline adopted 4-bounce channel-cut Si (111) monochromator for mono-beam X-ray nanodiffraction and X-ray absorption spectroscopy. The end-station is equipped with three ionization chambers and Lytle/SDD detector after the focusing position of KB mirror for transmission and fluorescence mode X-ray absorption spectroscopy. The photon flux on the sample ranges from 1×10^{11} ~ 3×10^{9} photon/sec for X-ray energy from 6 ~27 keV. The samples were scanned from 5 ~22 keV using transmission mode, and multiple patterns were collected for the sample. A metallic copper foil standard was used as a reference for energy calibration and was measured simultaneously with experimental samples. All the X-ray absorption spectra were collected at room temperature for each sample. The obtained XAFS data was processed in Athena (version 0.9.26) for background, pre-edge line and post-edge line calibrations. Then Fourier transformed fitting was carried out in Artemis (version 0.9.26). The FEFF programs were based on cif documents of CuBDC (CCDC: 687690). Prior to merging, spectra were calibrated against the reference spectra and aligned to the first peak in the smoothed first derivative of the absorption spectrum, the background noise was removed, and the spectra were processed to obtain a normalized unit edge step. The k^3 weighting, k range of 3 ~ 14 $Å^{-1}$ and R range of 1 ~ 3 Å were used for the fitting of Cu foil; k range of 3 ~ 11 $Å^{-1}$ and R range of 1 ~ 3 Å were used for the fitting of samples (crystalline CuBDC, CuPDC and amorphous CuPDC). Some of the parameters, coordination number, bond lengths were fixed, while Debye-Waller factor, E_0 shift were fitted without fixed, the $σ^2$ was set.

Catalytic performance measurement

CO_2 cycloaddition reactions with epoxides

In general, 10 mg catalysts, 0.25 mmol co catalyst (TBAB) and 12.5 mmol styrene oxide (SO) were added in a 20 mL sealed Schleck tube. The reactor was purged with pure CO_2 and vacuumed for several times to allow pure CO_2 atmosphere for the reaction. Then the catalytic cycloaddition reaction was carried out at a certain temperature via conventional thermo-catalysis. The CO_2 pressure was kept under 1 bar during the whole reaction. Typically, the catalytic reactions were last

for 8 h. After CO_2 cycloaddition reaction, the mixture solution needed centrifugation (10000 rpm, 10 min) to separate the catalyst, and the supernates were diluted in toluene and extracted by deionized water for three times to remove TBAB. Subsequently, anhydrous Na_2SO_4 was added to eliminate remnant water. After that, the solutions were filtrated and added dodecane as an internal standard before being investigated by Gas Chromatography (GC) analyses, which were performed on an equipment Fuli GC 9790 Plus, an instrument with FID detector with HP-5 capillary column. The substances were confirmed by gas chromatograph-mass spectrometer (GC/MS, Agilent 7890B-5977A). In addition, the catalysts after catalysis were washed with anhydrous methanol for three times, and then dried in a vacuum oven overnight at 50 °C. However, when measuring kinetic curves about CO_2 cycloaddition catalytic activity, the reaction solution was taken out in certain time intervals, purified with filtration and then measured by GC.

Recyclability investigation

After the first reaction of CO_2 cycloaddition with CO_2 and SO, the catalyst was separated, washed and dried before recyclability Then, a similar procedure was repeated five times to test the recyclability and stability of fabricated catalysts in the pure CO_2 atmosphere while other conditions were identical. The yield of SC was determined by GC. After circulations, the catalysts were collected and dried for XRD, and SEM examination to further confirm the stability of catalysts.

Kinetic study

To understand the process of reaction and further investigate the mechanism of cyclic carbonate synthesis, a dynamic model was established to investigate the kinetics for the cycloaddition reaction of SO and CO_2 over various catalysts.[1-3]

$$Rate=-d[SO]/dt=k[SO]^a \cdot [CO_2]^b \qquad \text{(Eq. S1)}$$

Where -d[SO], dt and k represnet the amount of SO consumed, the reaction time and the rate constant, respectively. a, b and c are the orders of the reaction. The values were determined as follows.

Since the pressure of CO_2 during the reaction was treated as a constant, b=1. And previous work has shown that the reaction is first order with respect to the epoxide concentration.[4-6] Therefore, assuming that the reaction is a first order reaction, a=1. Thus, the experimental rate equation was written as follows:

$$Rate=k' \cdot [SO]^1 \qquad \text{(Eq. S2)}$$

k' was calculated from the gradient of $\ln[1/(1-x)]$ *vs.* reaction time (t), where x represents the conversion of SO that can be determined by GC test. Moreover, the activation energy for the cycloaddition reaction can be calculated from the Arrhenius equation Equation (S3):

$$k'=A \cdot \exp(-E_a/RT) \qquad \text{(Eq. S3)}$$

where A and E_a were represented as the pre-exponential factor (min^{-1}) and the apparent activation energy (kJ mol^{-1}), respectively. R is the universal gas constant (8.314 J mol^{-1} K^{-1}), and T is the absolute temperature (K).

Building on the kinetic model treated by steady-state approximation method, the activation energy for CO_2 cycloaddition reaction catalyzed by different MOF catalysts were determined as follows:

$$\ln k' = \ln A - E_a/RT \qquad \text{(Eq. S4)}$$

where reaction temperatures (T) were in the range of 313~363 K by fitting the data from a plot of the natural logarithm of the observed first-order rate constant ($\ln k'$) against the reciprocal of the absolute temperature (1/T).

Additional Figures and Tables
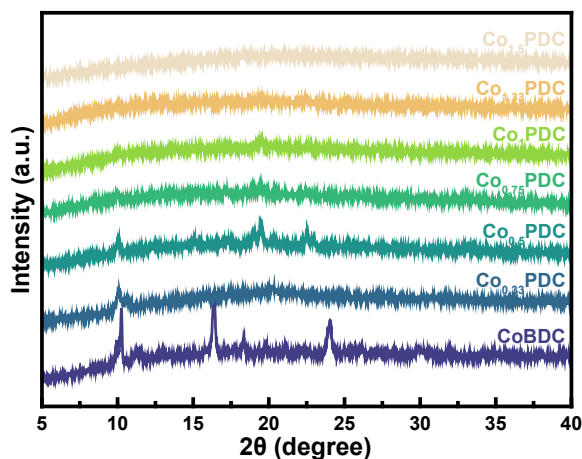
Fig S1. XRD patterns of CoBDC and a series of Co_xPDC MOF (x=0.33~1.5).

Interpreting the XRD patterns for the prepared Co_xPDC (x=0.33-0.75) MOFs shows a similar phase structure as referenced CoBDC, demonstrating the successful synthesis of CoPDC. There are three evident peaks at 9.19°, 18.36° and 22.23° corresponding to (200), (400) and (202) crystal facets, respectively. The other two characteristic XRD signals at 10.04°, 19.48° correspond to the (101), (002) crystalline planes of fabricated CoPDC MOF(CCDC: 265093). With the increment of cobalt salts, the crystallinity of CoPDC MOFs was transformed from crystalline to amorphous state, which displayed a similar trend as CuPDC. The loss of long-distance order as indicated by XRD patterns also confirms the effective ligands' adjustment influence on the amorphization.

Table S1. ICP results and elemental analysis of Cu_xPDC MOF (x=0.33~1.5)

Sample	Content of Cu[a] [mg/mg$_{sample}$]	Content of N[a] [mg/mg$_{sample}$]	Molar ratio of Cu/N	Theoretical value of Cu/N
$Cu_{1.5}PDC$	0.2125	0.0763	0.6092	0.75
$Cu_{1.33}PDC$	0.216	0.0853	0.5539	0.665
Cu_1PDC	0.2136	0.0962	0.4857	0.5
$Cu_{0.75}PDC$	0.1875	0.110	0.3729	0.375
$Cu_{0.5}PDC$	0.1723	0.146	0.2581	0.25
$Cu_{0.33}PDC$	0.1798	0.195	0.2017	0.165

[a] The content of Cu and N was obtained via ICP test and elemental analysis detection, respectively.

Table S2. ICP results and elemental analysis of Co_xPDC MOF (x=0.33~1.5)

Sample	Content of Co [mg/mg$_{sample}$][a]	Content of N [mg/mg$_{sample}$][a]	Molar ratio of Co/N	Theoretical value of Co/N
$Co_{1.5}PDC$	0.4070	0.1485	0.6511	0.75
$Co_{1.33}PDC$	0.4933	0.1897	0.6177	0.665
Co_1PDC	0.2651	0.1293	0.4871	0.5
$Co_{0.75}PDC$	0.2593	0.1690	0.3645	0.375
$Co_{0.5}PDC$	0.2565	0.2789	0.2185	0.25
$Co_{0.33}PDC$	0.3928	0.6365	0.1466	0.165

[a] The content of Co and N was obtained via ICP test and elemental analysis detection, respectively.
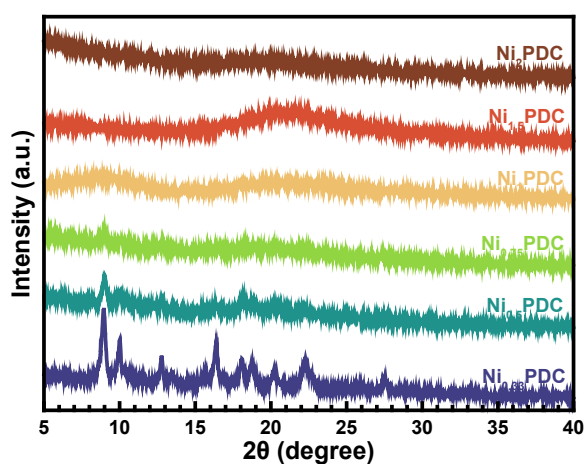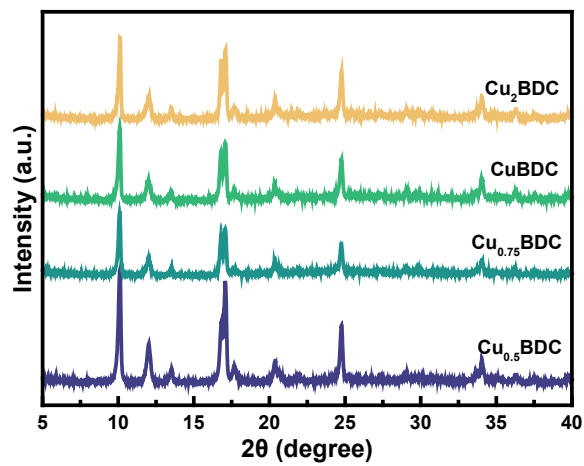

Fig S2. XRD patterns of Ni_xPDC MOF (x=0.33~1.5).
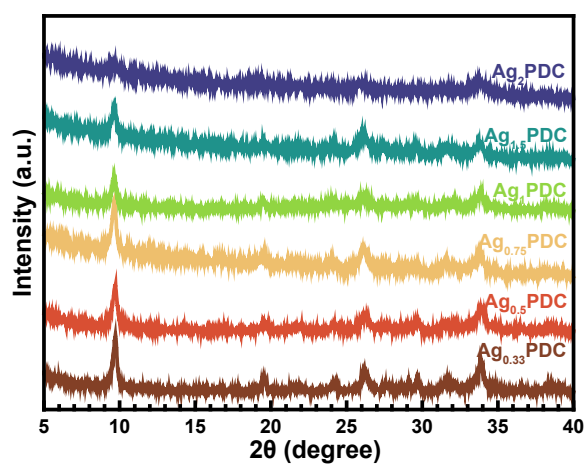
Fig S3. XRD patterns of Ag_xPDC MOF (x=0.33~1.5).
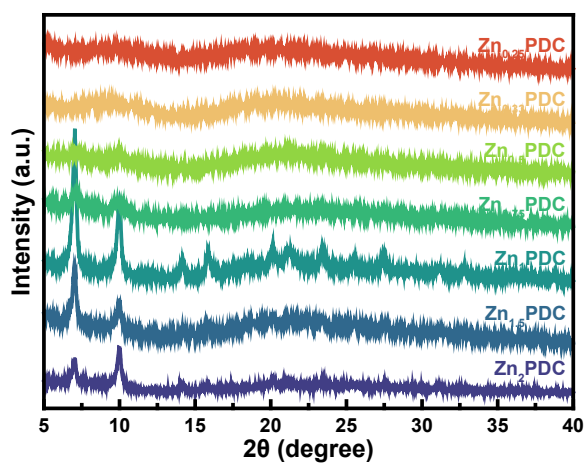
Fig S4. XRD patterns of ZnxPDC MOF (x=0.25~2).


Fig S5. XRD patterns of Cu_xBDC (x=0.5~2) with different ratios of Cu cations and organic linkers (BDC).

Table S3. Results of the curve-fit parameters executed on the k^3-weighted FT-EXAFS spectra of aCuPDC, cCuPDC and cCuBDC MOFs

| Sample	Path	S_0^2	N	R(Å)	σ^2 (Å^2)	ΔE_0	R factor
aCuPDC	Cu-O$_1$		3.8±0.2	1.96±0.01	0.0073		
	Cu-O$_2$	0.85	1	2.15±0.03	0.0035	-1.9±0.8	0.0179
	Cu-Cu		1.2±0.2	2.89±0.04	0.0198		
cCuPDC	Cu-O$_1$		4.0±0.1	1.95±0.01	0.0072		
	Cu-O$_2$	0.88	1	2.15±0.02	0.0021	8.3±1.5	0.0116
	Cu-Cu		1	2.88±0.03	0.0026		
cCuBDC	Cu-O$_1$		4.1±0.3	1.96±0.01	0.0087		
	Cu-O$_2$	0.9	1	2.15±0.03	0.0033	5.1±1.0	0.0170
	Cu-Cu		1.2±0.1	2.64±0.02	0.0029		
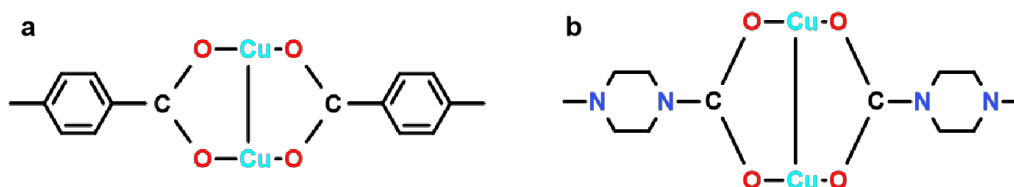
Fig S6. Schematic plots of microstructure differences between a) cCuBDC and b) aCuPDC MOF.
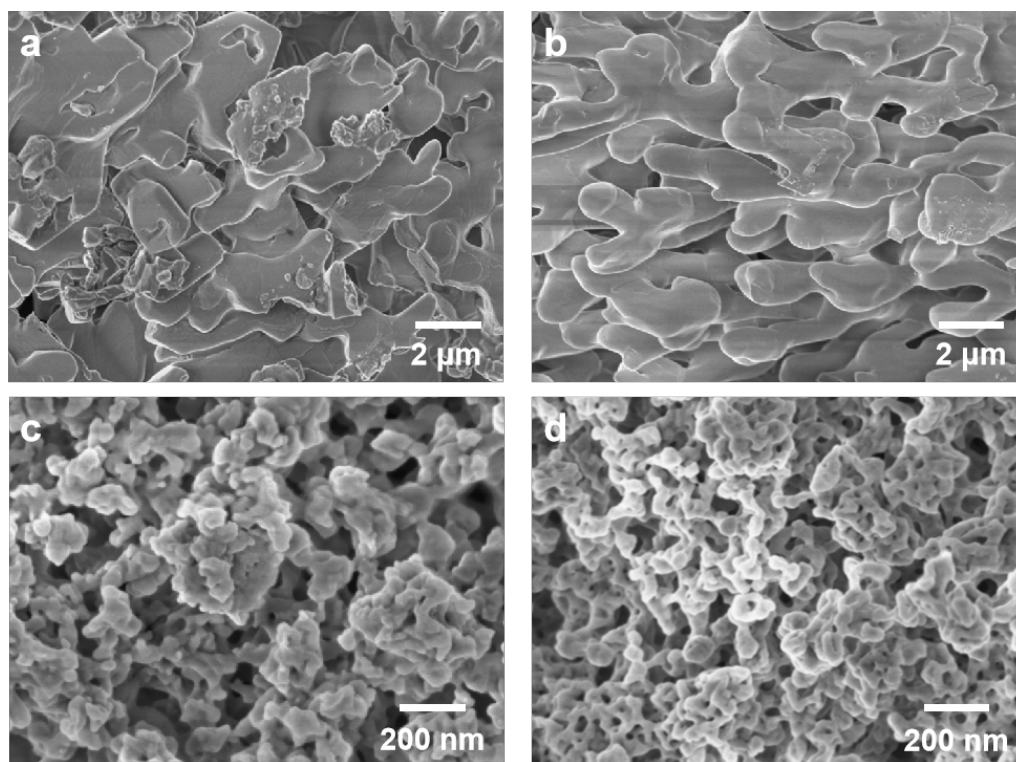
Fig S7. SEM images of Cu$_x$PDC (x=0.33~1.5) MOF. a) Cu$_{0.33}$PDC, b) Cu$_{0.75}$PDC, c) Cu$_{1.33}$PDC, d) Cu$_{1.5}$PDC.
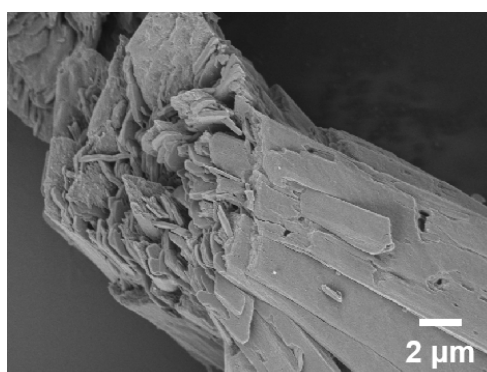
Fig S8. SEM image of CoBDC MOF.
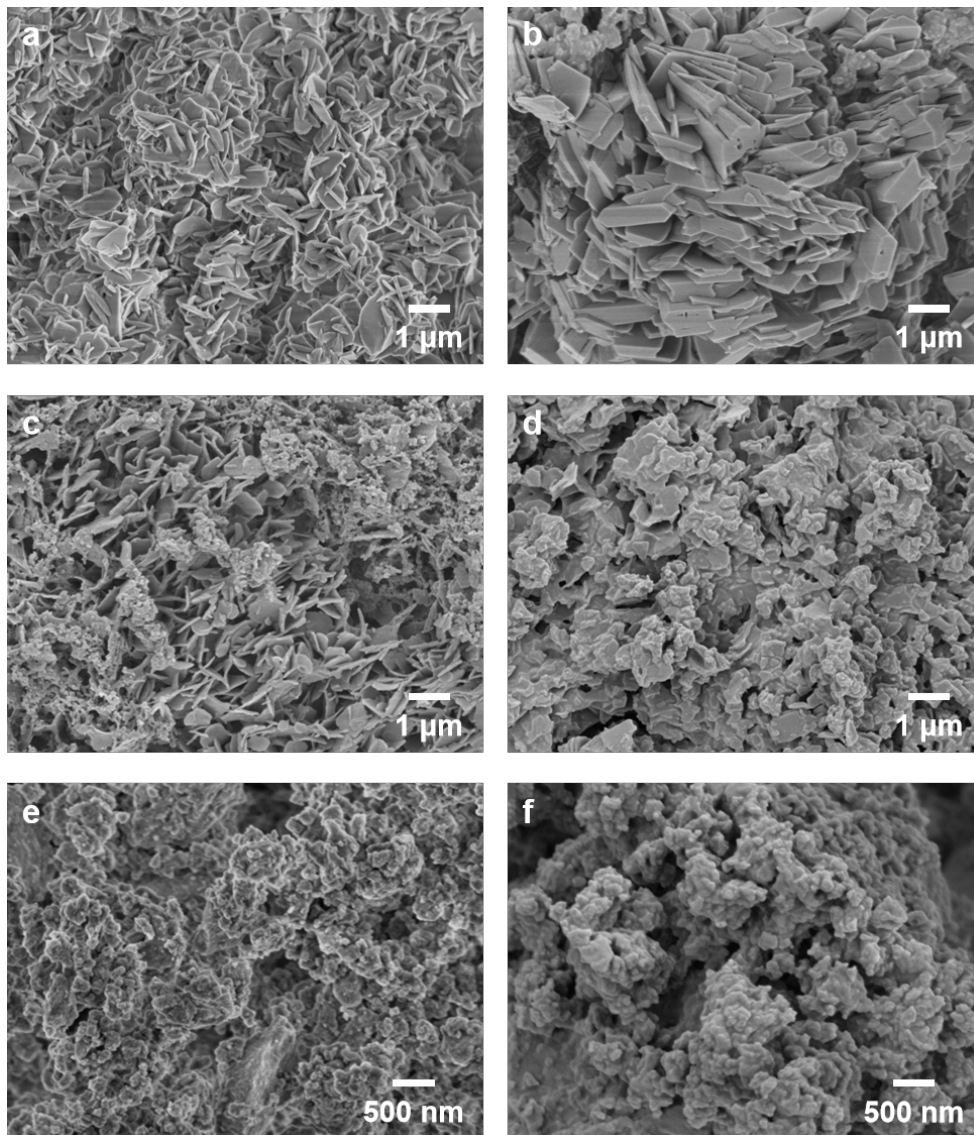
Fig S9. SEM images of Co_xPDC (x=0.33~1.5) MOF. a) $Co_{0.33}PDC$, b) $Co_{0.5}PDC$, c) $Co_{0.75}PDC$, d) Co_1PDC, e) $Co_{1.33}PDC$, f) $Co_{1.5}PDC$.

SEM images displayed the crystalline CoPDC MOFs have sheet microstructure, which were similar to the referenced CoBDC MOFs. With the growing concentration of metal sites, small irregular particles have appeared in the SEM images of amorphous samples and the amount of these particles showed an upward trend. The irregular particles were attributed to the elaborate structure of amorphous materials. Thus, two characteristic samples, a crystalline CoPDC ($Co_{0.5}PDC$, named cCoPDC), amorphous CoPDC (Co_1PDC, named aCoPDC) and referenced crystalline CoBDC (named cCoBDC) were chosen to accomplish a series of characterization and test.
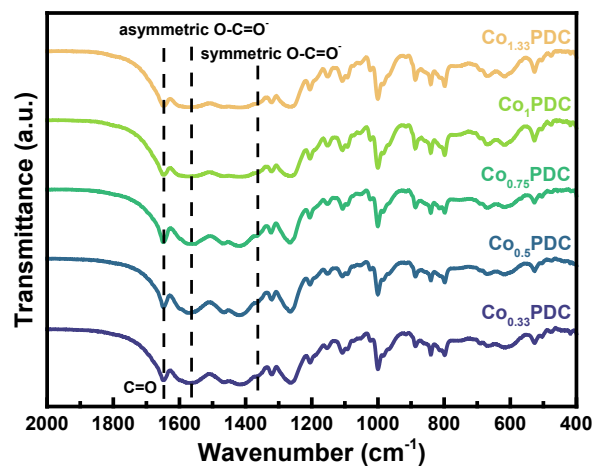
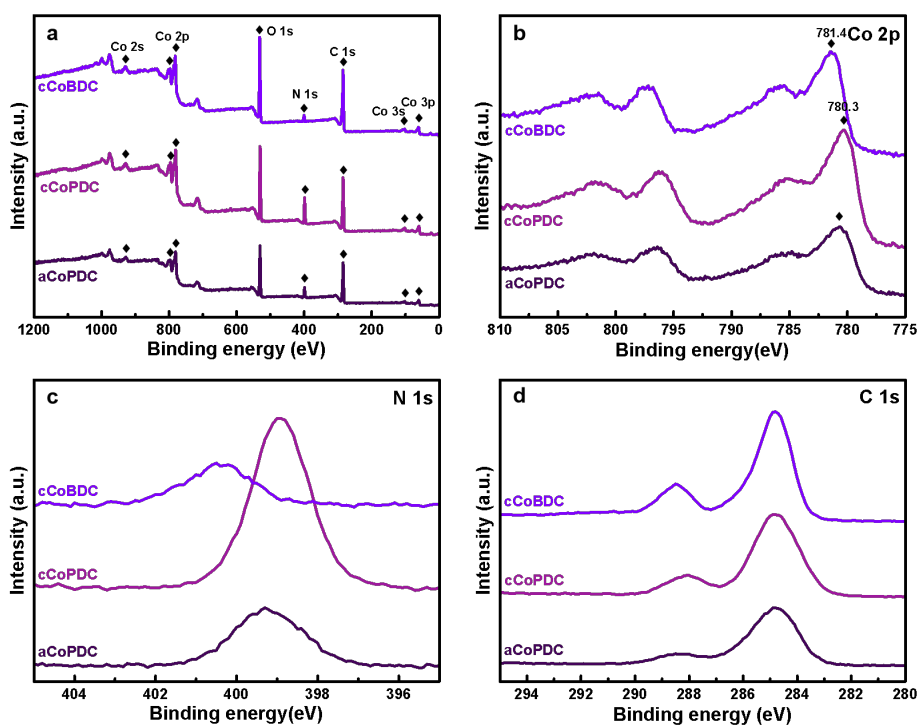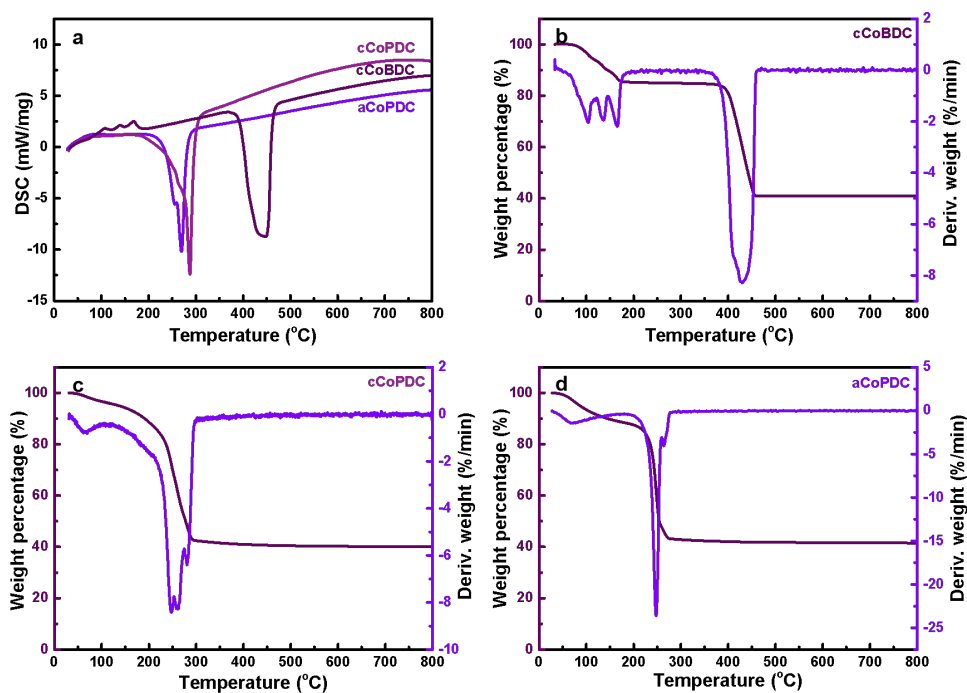**Fig S10.** FTIR spectra of Co_xPDC MOF (x=0.33~1.5).

Fig S11. a) The XPS wide spectra of cCoBDC, cCoPDC and aCoPDC MOF. The XPS spectra of high-resolution of b) Co 2p, c) N 1s, d) C 1s for cCoBDC, cCoPDC and aCoPDC.

Fig S12. a) DTG and TGA curves of b) cCoBDC, c) cCoPDC and d) aCoPDC MOFs.

There were two obvious weight-loss stages in cCoBDC, the first process contained the temperature from 50 °C to 200 °C, and the appeared peaks were assigned to the adsorbate (like H_2O) volatilization and removal of solvent (DMF). Besides, the second stage included another broad peak existed at the temperature around 425 °C, demonstrating the complete pyrolysis of MOF's framework structure. By contrast, cCoPDC MOF was totally destroyed at 290 °C while aCoPDC collapsed at 285 °C, indicating better thermal stability of aCoPDC compared with cCoPDC. Therefore, the amorphization process negligibly affected the thermal stability in CoPDC MOFs.
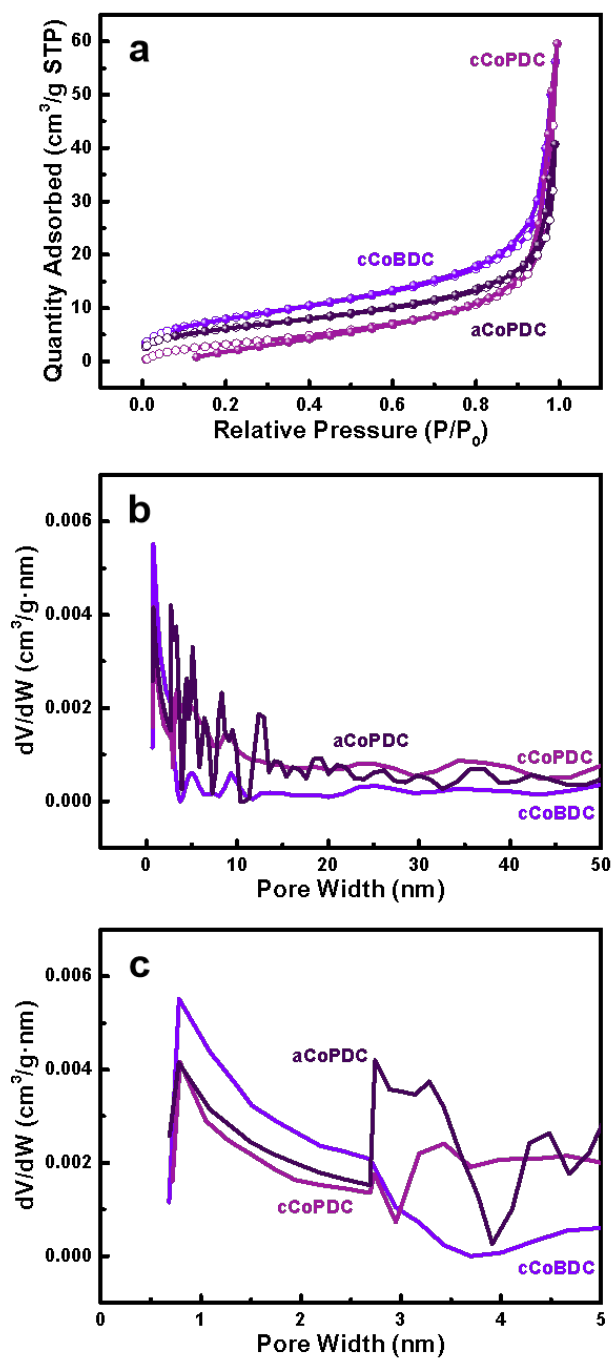
Fig S13. a) N$_2$ sorption isotherms at 77 K, b)- c) Pore size distribution based on the DFT method for cCuBDC, cCuPDC and aCuPDC, respectively.
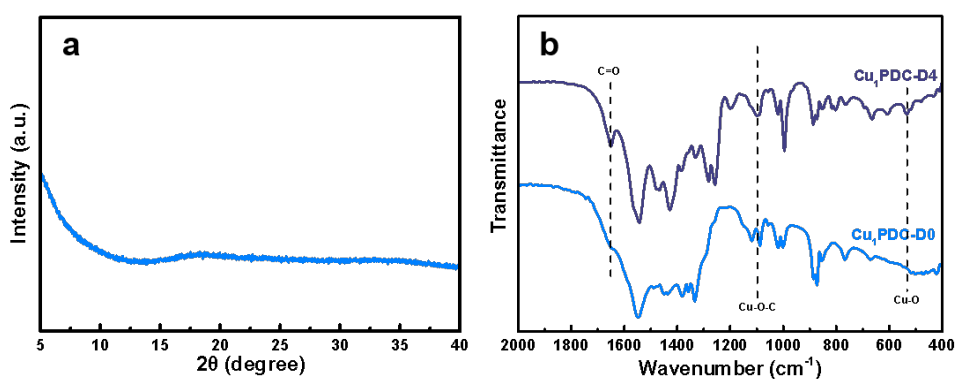
Fig S14. a) XRD pattern of Cu$_1$PDC-D0. b) FTIR spectra of Cu$_1$PDC-D0 and Cu$_1$PDC-D4.

The characteristic peaks at 1650 cm^{-1}, 1100 cm^{-1} and 536 cm^{-1} disappeared in Cu$_1$PDC-D0. The bending vibration at 1650 cm^{-1} is represented to the C=O group, while the peaks at 536 cm^{-1} and 1100 cm^{-1} are assigned to Cu-O bonds and Cu-O-C bonds, respectively. The results implied there were no relative bonds that belonged to CuPDC MOF formed.

Table S4. ICP results and elemental analysis of Cu$_1$PDC-Dn MOFs (n=0~8, representing the molar ratio of DBU to PDC)

Sample	Content of Cu [mg/mg$_{sample}$][a]	Content of N [mg/mg$_{sample}$][a]	Molar ratio of Cu/N	Theoretical value of Cu/N
Cu$_1$PDC-D0	0.4911	0.1765	0.6087	0.5
Cu$_1$PDC-D1	0.3502	0.1556	0.4923	0.5
Cu$_1$PDC-D2	0.4834	0.2019	0.5237	0.5
Cu$_1$PDC-D4	0.4028	0.1837	0.4796	0.5
Cu$_1$PDC-D6	0.5204	0.2239	0.5084	0.5
Cu$_1$PDC-D8	0.3766	0.1702	0.4840	0.5

[a] The content of Co and N was obtained via ICP test and elemental analysis detection, respectively.
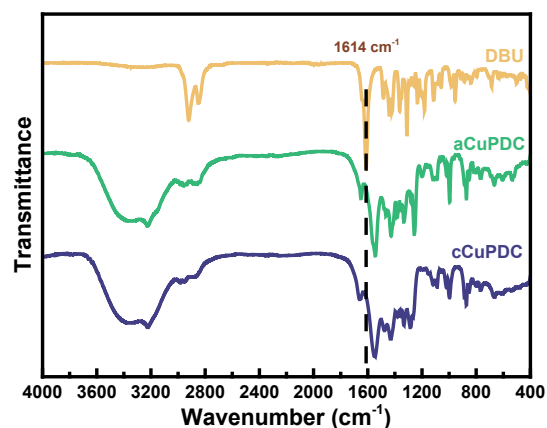
Fig S15. The FTIR spectra of DBU, cCuPDC and aCuPDC.

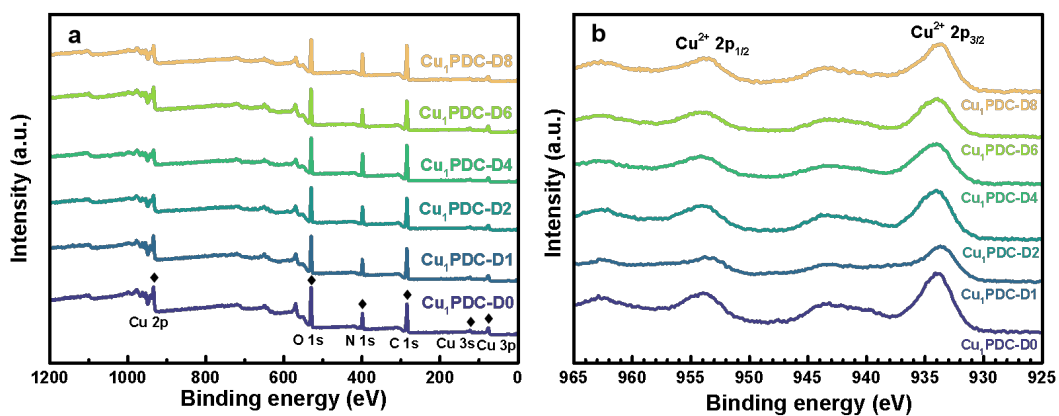**Fig S16.** a) The XPS wide spectra of $Cu_1PDC-Dn$ (n=0~8, representing the molar ratio of DBU to PDC) MOFs. b) The XPS spectra of high-resolution of Cu 2p.
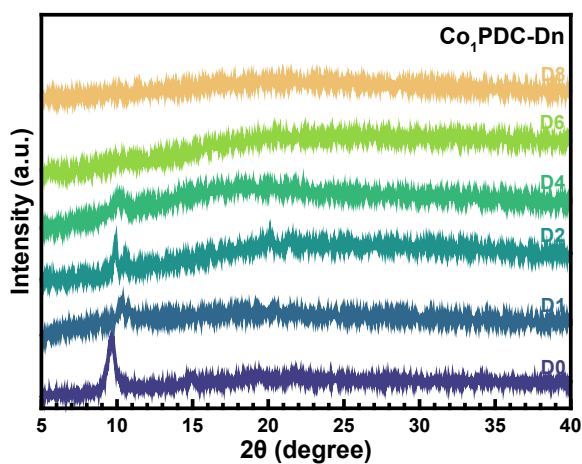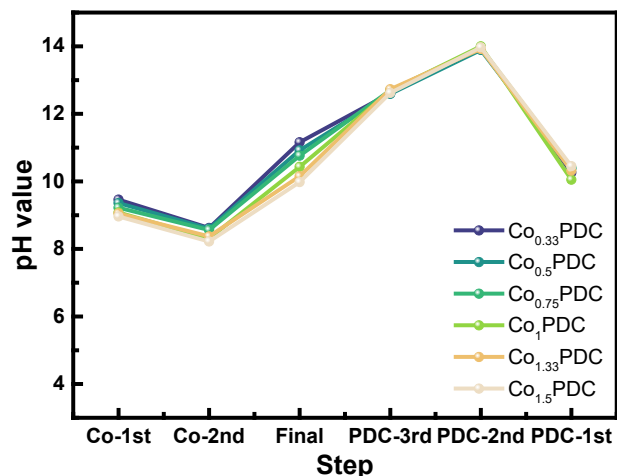

Fig S17. XRD patterns of $Co_1PDC-Dn$ (n=0~8, representing the molar ratio of DBU to PDC) MOFs.

Fig S18. The pH value of solution in every step. The corresponding substances in individual steps are:

Co-1st: pristine $Co(OAc)_2$ solution under Ar atmosphere; Co-2nd: $Co(OAc)_2$ solution under CO_2 atmosphere; PDC-1st: pristine H_2PZ solution under Ar atmosphere; PDC-2nd: H_2PZ solution after adding DBU modulators under Ar atmosphere; PDC-3rd: the obtained solution in PDC-2nd step but purged with excessive CO_2; Final: solution of generated product (CoPDC MOF) through mixing solution of Co-2nd and PDC-3rd.
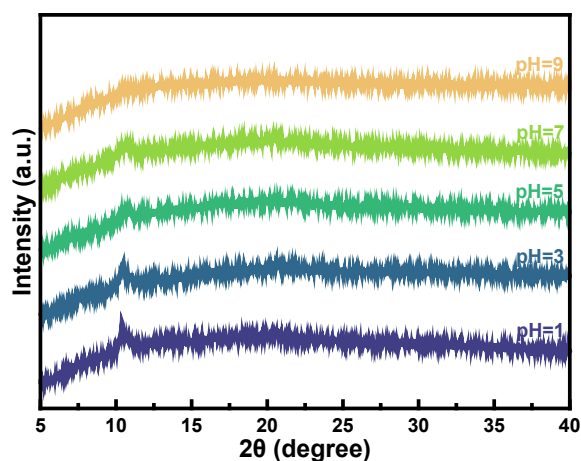
Fig S19. XRD patterns of Co_1PDC-D4 with different pH values of solution (pH=1, 3, 5, 7, 9). The pH value was adjusted by adding various amounts of HCl modulators in the metal ions' solution.

Table S5. Quantitative analysis of Lewis acid and base sites from CO_2-TPD and NH_3-TPD results

Samples	Amount of Lewis acid sites [mmol/g]	Amount of Lewis base sites [mmol/g]
cCuBDC	2.75	1.09
cCuPDC	2.82	1.56
aCuPDC	2.95	1.76

Table S6. A list of catalytic performance and reaction conditions of reported copper-based catalysts for the cycloaddition with SO in pure CO_2 atmosphere.

Catalyst	Co-catalyst	T (°C)	P [atm]	Time [h]	Yield [%]	TON	TOF	Ref.
Cu(L)(A)	TBAB	90	1	24	90.2	909	37.9	[7]
[Cu$_{12}$] nanocages	TBAB	60	1	12	99	247.5	20.6	[8]
Cu(□)-MOG	TBAB	27	1	48	62	310	6.5	[9]
JLU-Liu20	TBAB	80	1	48	72	288	6	[10]
JLU-Liu21	TBAB	80	1	48	90	360	7.5	[10]
JLU-Liu22	TBAB	80	1	48	65	260	5.4	[10]
JLU-Liu46	TBAB	80	1	48	68	272	5.7	[10]
Cu$_2$(CPTPTA)	TBAB	60	20	6	65	130	21.7	[11]
FJI-H14	TBAB	80	0.15	24	86	179	7.5	[12]
HKUST-1	TBAB	80	0.15	24	67	140	5.8	[13]
Cu$_2$(ABTC)	TBAB	60	1	8	90	180	22.5	[13]
CuBDC	TBAB	60	1	8	68	136	17	[13]
PNU-25-NH$_2$	TBAB	55	1	18	35	35	1.9	[14]
HNUST-9	TBAB	80	1	48	44.3	591	12.3	[15]
HKUST-1	TBAB	28	1	48	47	16	0.3	[16]
Porphyrin-based Cu-1a MOF	TBAB	28	1	48	52	18	0.4	[16]
Porphyrin-based Cu-1b MOF	TBAB	28	1	48	66	23	0.5	[16]
Cu-MOF	/	90	1	5	15.7	4	0.7	[17]
Ch@UiO-67	TBAI	70	10	6	93	37	6.2	[18]
Cu$_7$(H$_1$L)$_2$(TPT)$_3$	TBAB	100	10	12	99	1429	119	[19]
Cu$_6$(L)$_3$	TBAB	25	1	8	89	445	55.6	[20]
1a	TBAB	100	10	6	64.1	1282	214	[21]
Cu(C$_{14}$H$_8$O$_6$)	TBAB	25	1	18	85	497	27.6	[22]
CSMCRI-13(13a)	TBAB	70	8	6	94.5	672	111.9	[23]

Catalyst	Co-catalyst	T (ºC)	P [atm]	Time [h]	Yield [%]	TON	TOF	Ref.
Cu-TABC	TBAB	25	1	48	46.6	26	0.5	[24]
$Cu^I_3Cu^{II}_2(OH)pz6$	TBAB	25	1	24	92	153	6.4	[25]
CuTrp	TBAB	100	12	9	81.5	98	10.9	[26]
$Cu_2(4\text{-}TPOM)(3,7\text{-}DBTDC)_2$	TBAB	28	1	24	11	64	2.7	[27]
$Cu_xO_y@COF$	TBAB	35~40	1	12	92	230	19.2	[28]
Cu-ABF@ASMNPs	DBU	80	1	12	92	70	5.8	[29]
Cu/POP-Bpy	Bu_4NBr	80	1	48	86.2	172	3.6	[30]
BIT-C	Bu_4NBr	60	1	6	99	99	16.5	[31]
SSICG-1	TBAB	120	1	12	87	174	14.5	[32]
Cu-URJC-8	TBAB	25	12	24	47	47	2	[33]
Cu-URJC-1	TBAB	25	12	24	52	2544	106	[34]
JUC-62	TBAB	25	12	24	46	1848	77	[34]
HNUST-1	TBAB	25	12	24	34	1728	72	[34]
Cu-MOF-74	TBAB	25	12	24	32	1104	46	[34]
HKUST-1	TBAB	25	12	24	27	840	35	[34]
PCN-16	TBAB	25	12	24	19	792	33	[34]
aCoPDC	TBAB	70	1	12	99.5	2640	220	This work
aCuPDC	TBAB	70	1	12	99	2627	218.9	This work
cCuPDC	TBAB	70	1	12	86.4	2465	205.4	This work

Turnover frequency: TOF value is determined by Equation S5-S6, which is the essential parameter to evaluate the performance of fabricated catalysts.

TOF= TON value/reaction time (h)   (Eq. S5)

TON= product (mmol)/active sites (mmol)   (Eq. S6)

where the number of active sites were confirmed by ICP results in **Table S5**.
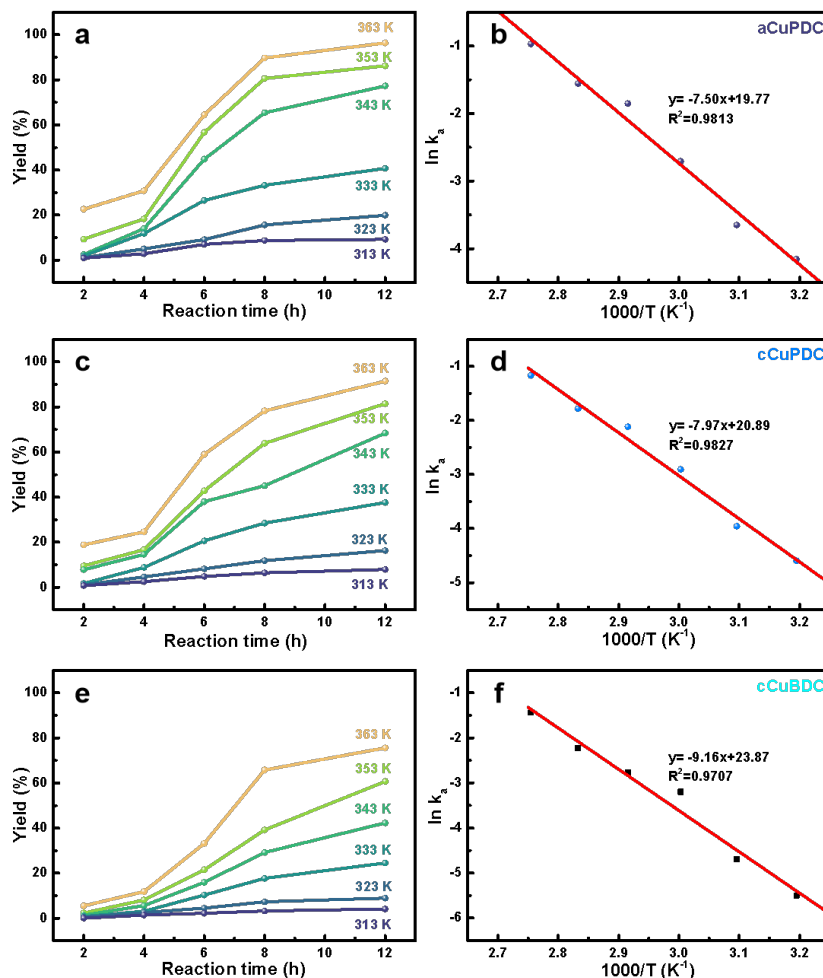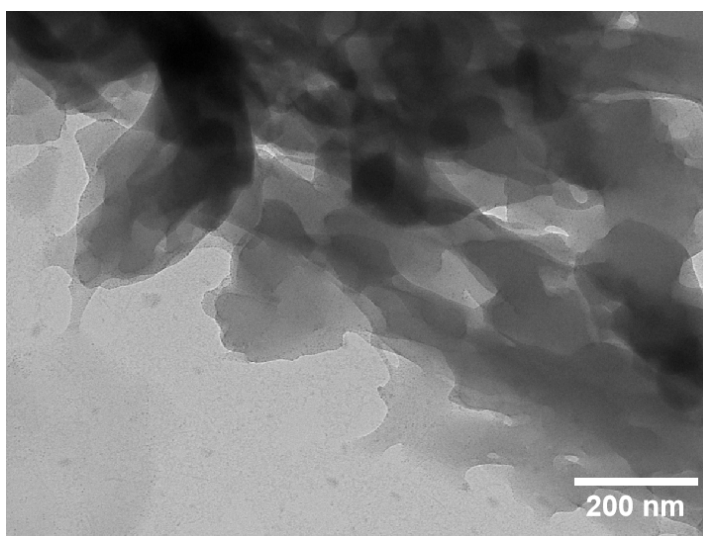
Fig S20. a) The yield of SC from cycloaddition of styrene oxide and CO_2 catalyzed by aCuPDC MOF under different reaction temperatures from 313 K~363 K. b) Arrhenius plots of $\ln k_a$ against the reciprocal absolute temperature (1/T) for the apparent activation energy of aCuPDC. c) The yield of SC from cycloaddition of styrene oxide and CO_2 catalyzed by cCuPDC MOF under different reaction temperatures from 313 K~363 K. d) Arrhenius plots of $\ln k_a$ against the reciprocal absolute temperature (1/T) for the apparent activation energy of cCuPDC. e) The yield of SC from cycloaddition of styrene oxide and CO_2 catalyzed by cCuBDC MOF under different reaction temperatures from 313 K~363 K. f) Arrhenius plots of $\ln k_a$ against the reciprocal absolute temperature (1/T) for the apparent activation energy of cCuBDC.
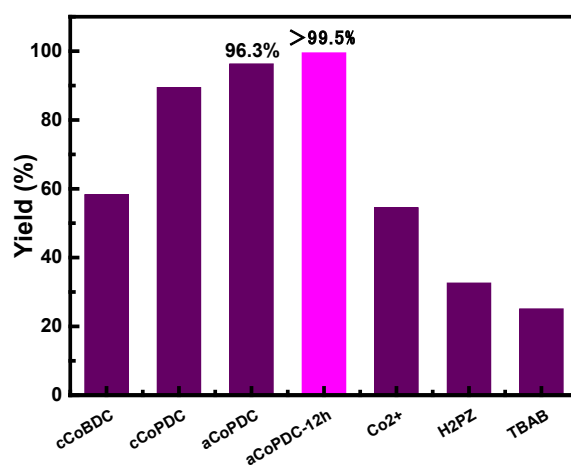
Reaction conditions: 10 mg catalyst, 0.25 mmol co-catalyst (TBAB) and 12.5 mmol SO, 6 mL toluene, 1 bar CO_2.
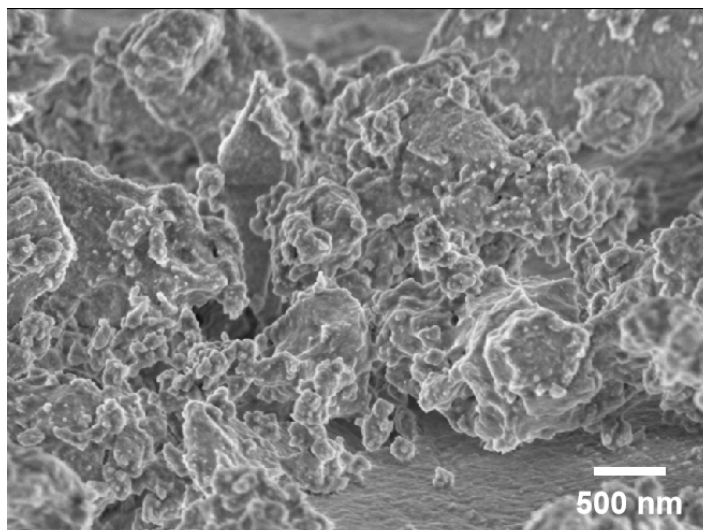
Fig S21. SEM image of aCuPDC after cyclic catalysis.

Fig S22. TEM image of aCuPDC after catalysis.


Fig S23. Cycloaddition reaction of CO_2 with SO catalyzed by different catalysts. Reaction conditions: 10 mg catalyst, 0.25 mmol co-catalyst (TBAB) and 12.5 mmol SO, 343 K, 1 bar CO_2, 8 h (except aCoPDC-12h).
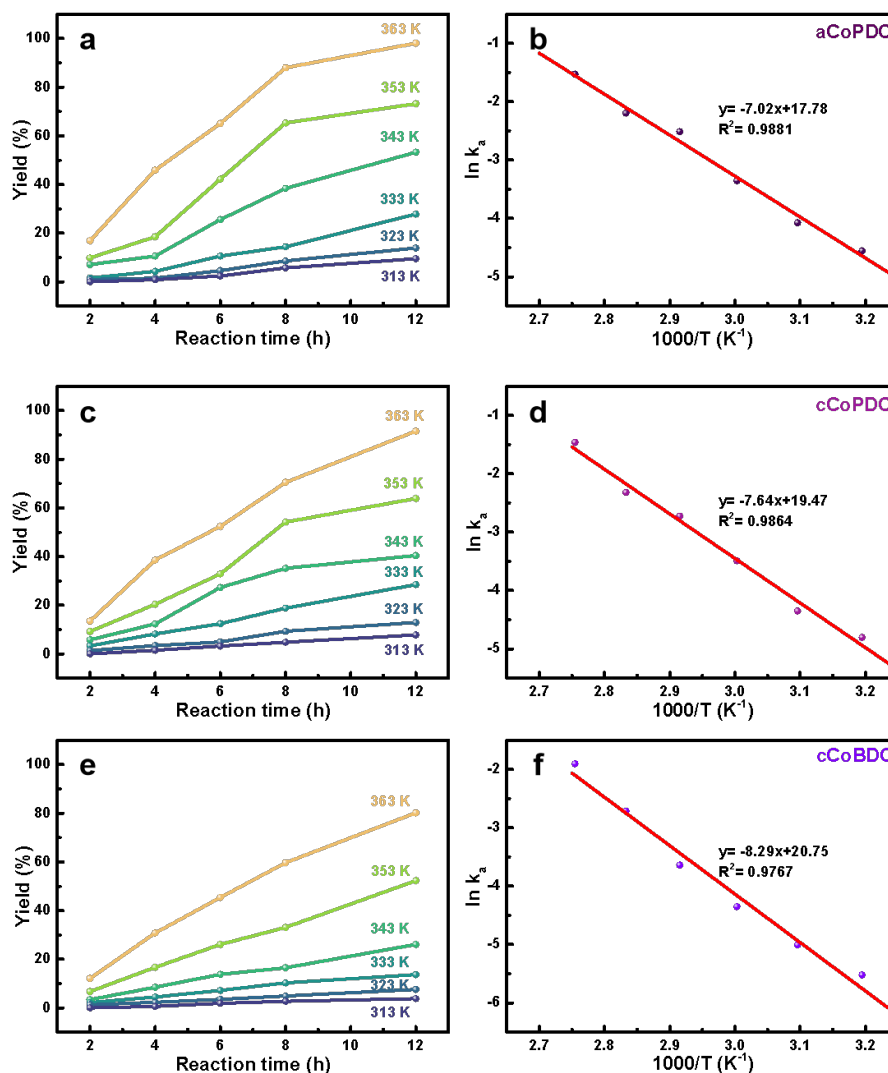
Fig S24. a) The yield of SC from cycloaddition of styrene oxide and CO_2 catalyzed by aCoPDC MOF. b) Arrhenius plots of $\ln k_a$ against the reciprocal absolute temperature (1/T) for the apparent activation energy of aCoPDC. c) The yield of SC from cycloaddition of styrene oxide and CO_2 catalyzed by cCoPDC MOF. d) Arrhenius plots of $\ln k_a$ against the reciprocal absolute temperature (1/T) for the apparent activation energy of cCoPDC. e) The yield of SC from cycloaddition of styrene oxide and CO_2 catalyzed by cCoBDC MOF. f) Arrhenius plots of $\ln k_a$ against the reciprocal absolute temperature (1/T) for the apparent activation energy of cCoBDC.

Reaction conditions: 10 mg catalyst, 0.25 mmol co-catalyst (TBAB) and 12.5 mmol SO, 6 mL toluene, 1 bar CO_2.
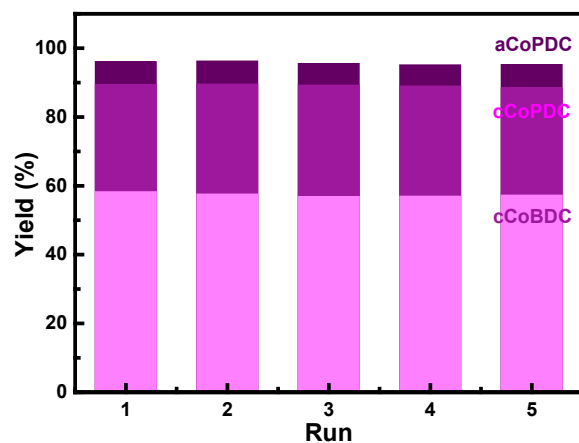
Fig S25. Catalytic stability of cCoBDC, cCoPDC and aCoPDC MOF.
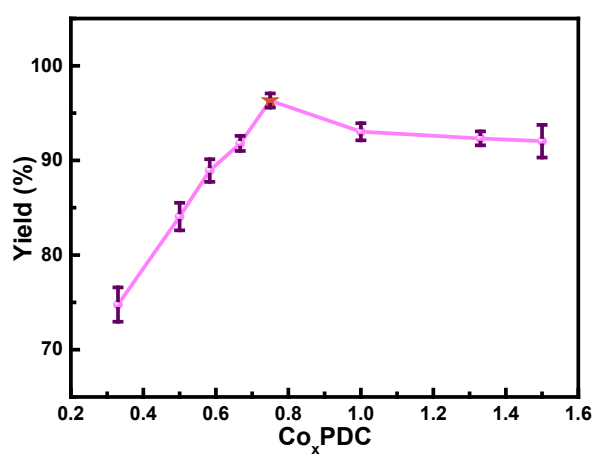
Fig S26. The yield of SC catalyzed by a series of Co_xPDC MOFs (x=0.33~1.5). Reaction conditions: 10 mg catalyst, 0.25 mmol TBAB, 12.5 mmol SO, 343 K, 1 bar CO_2, 8 h.
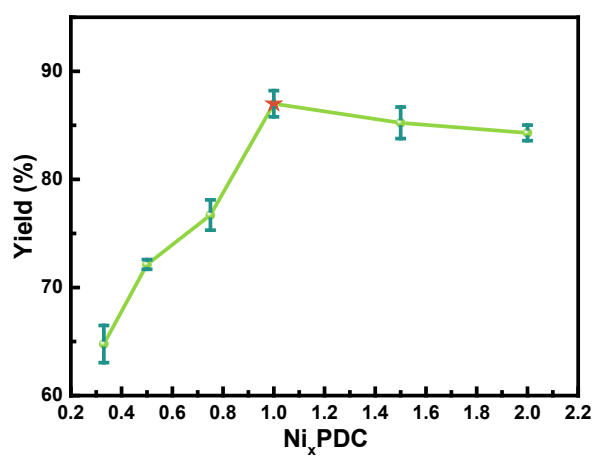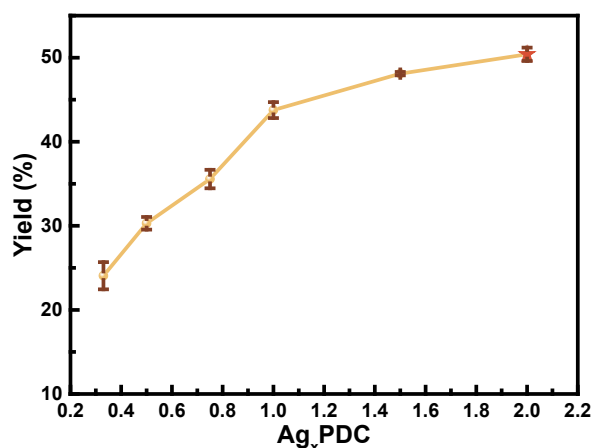

Fig S27. The yield of SC catalyzed by a series of Ni_xPDC MOFs (x=0.33~2). Reaction conditions: 10 mg catalyst, 0.25 mmol TBAB, 12.5 mmol SO, 343 K, 1 bar CO_2, 8 h.
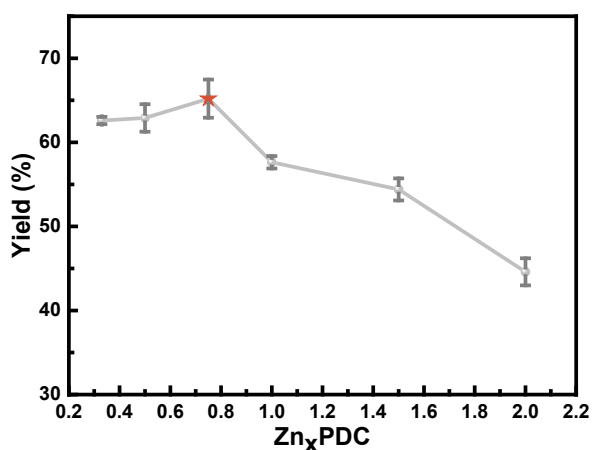
Fig S28. The yield of SC catalyzed by a series of Ag_xPDC MOFs (x=0.33~2). Reaction conditions: 10 mg catalyst, 0.25 mmol TBAB, 12.5 mmol SO, 343 K, 1 bar CO_2, 8 h.

Fig S29. The yield of SC catalyzed by a series of Zn_xPDC MOFs (x=0.25~2). Reaction conditions: 10 mg catalyst, 0.25 mmol TBAB, 12.5 mmol SO, 343 K, 1 bar CO_2, 8 h.

Density Functional Theory (DFT) calculation

All calculations were performed by the open source software CP2K package [35]. PBE functional attached D3 correction was used to describe the system [36]. In the framework of the Gaussian and plane waves method, Kohn-Sham DFT was utilized as the electronic structure method [37]. The Goedecker-Teter-Hutter (GTH) pseudopotentials, DZVP-MOLOPT-SR-GTH basis sets were used separately to describe the molecules [38-39]. A plane-wave energy cut-off of 500 Ry and relative cut-off of 60 Ry have been employed. The energy convergence criterion was set as 10^{-6} Hartree. The CuPDC (001) was selected as the absorbed slab to proceed the catalytic reactions in a $22.82 \times 28.53 \times 26.61$ Å^3 box under a periodic boundary condition with a vacuum layer of 15 Å in z axis. The free energy ΔG of each step for the whole reaction path could be calculated by the software Shermo[40] as follows:

$$\Delta G = \Delta E + (ZPE) - T\Delta S$$

References

1. R. Luo, W. Zhang, Z. Yang, X. Zhou, H. Ji, *J. CO₂ Util.*, 2017, **19**, 257-265.

2. A. Rehman, V. C. Eze, M. F. M. G. Resul, A. Harvey, *J. Energy Chem.*, 2019, **37**, 35-42.

3. F. Della Monica, B. Maity, T. Pehl, A. Buonerba, A. De Nisi, M. Monari, A. Grassi, B. Rieger, L. Cavallo, C. Capacchione, *ACS Catal.*, 2018, **8**, 6882-6893.

4. J. A. Castro-Osma, A. Lara-Sánchez, M. North, A. Otero, P. Villuendas, *Catal. Sci. Technol.*, 2012, **2**, 1021-1026.

5. A. Rehman, V. C. Eze, M. F. M. G. Resul, A. Harvey, *J. Energy Chem.*, 2019, **37**, 35-42.

6. A. Rehman, A. M. L. Fernández, M. F. M. Gunam Resul, A. Harvey, *J. CO₂ Util.*, 2018, **24**, 341-349.

7. K. Huang, Q. Li, X. Y. Zhang, D. B. Qin, B. Zhao, *Cryst. Growth Des.*, 2022, **22**, 6531-6538.

8. W. M. Wang, W. T. Wang, M. Y. Wang, A. L. Gu, T. D. Hu, Y. X. Zhang, Z. L. Wu, *Inorg. Chem.*, 2021, **60**, 9122-9131.

9. C. K. Karan, M. C. Sau, M. Bhattacharjee, *Chem. Commun.*, 2017, **53**, 1526-1529.

10. J. M. Gu, X. D. Sun, X. Y. Liu, Y. Yuan, H. Y. Shan, Y. L. Liu, *Inorg. Chem. Front.*, 2020, **7**, 4517-4526.

11. Y. Y. Zhu, J. M. Gu, X. Y. Yu, B. R. Zhang, G. H. Li, J. T. Li, Y. L. Liu, *Inorg. Chem. Front.*, 2021, **8**, 4990-4997.

12. L. F. Liang, C. P. Liu, F. L. Jiang, Q. H. Chen, L. J. Zhang, H. Xue, H. L. Jiang, J. J. Qian, D. Q. Yuan, M. C. Hong, *Nat. Commun.*, 2017, **8**, 1233.

13. P. T. K. Nguyen, Y B. N. Tran, *ChemistrySelect*, 2021, **6**, 4067-4073.

14. J. F. Kurisingal, Y. Rachuri, Y. J. Gu, R. K. Chitumalla, S. Vuppala, J. Jang, K. K. Bisht, E. Suresh, D.-W. Park, *ACS Sustain. Chem. Eng.*, 2020, **8**, 10822-10832.

15. J. X. Liao, We. J. Zeng, B. S. Zheng, X. Y. Cao, Z. X. Wang, G. Y. Wang Q. Y. Yang, *Inorg. Chem. Front.*, 2020, **7**, 1939-1948.

16. T. Murayama, M. Asano, T. Ohmura, A. Usuki, T. Yasui, Y. Yamamoto, *B. Chem. Soc. Jpn.*, 2018, **91**, 383-390.

17. A. G. Liu, Y. Chen, P. D. Liu, W. Qi, B. Li, *Inorg. Chem. Front.*, 2022, **9**, 4425-4432.

18. A. Helal, F. Alahmari, M. Usman, Z. H. Yamani, *J. Environ. Chem. Eng.*, 2022, **10**, 108061.

19. J. Ai, X. Min, C. Y. Gao, H. R. Tian, S. Dang, Z. M. Sun, *Dalton T.*, 2017, **46**, 6756-6761.

20. V. Sharma, D. De, R. Saha, R. Das, P. K. Chattaraj, P. K. Bharadwaj, *Chem. Commun.*, 2017, **53**, 13371-13374.

21. C. Y. Gao, H. R. Tian, J. Ai, L. J. Li, S. Dang, Y. Q. Lan, Z. M. Sun, *Chem. Commun.*, 2016, **52**, 11147-11150.

22. K. Manna, R. Kumar, A. Sundaresan, S. Natarajan, *Inorg. Chem.*, 2023, **62**, 13738-13756.

23. N. Seal, S. Neogi, *ACS Appl. Mater. Inter.*, 2021, **13**, 55123-55135.

24. S. Liu, L. H. Liu, L. Liu, Z. B. Han, *Catal. Lett.*, 2023, **153**, 2892-2899.

25. J. G. Wang, Y. Liu, C. M. Liu, J. H. Chen, G. Yang, *Dalton T.*, 2023, **52**, 9275-9281.

26. G. S. Jeong, A. C. Kathalikkattil, R. Babu, Y. G. Chung, D. W. Park, *Chinese J. Catal.*, 2018, **39**, 63-70.

27. G. Chakraborty, P. Das, S. K. Mandal, *Inorg. Chem.* 2021, **60**, 5071-5080.

28. M. Sengupta, A. Bag, S. Ghosh, P. Mondal, A. Bordoloi, Sk. M. Islam, *J. CO₂ Util.*, 2019, **34**, 533-542.

29. R. K. Sharma, R. Gaur, M. Yadav, A. Goswami, R. Zbořil, M. B. Gawande, *Sci. Rep.*, 2018, **8**, 1901.

30. Z. F. Dai, Q. Sun, X. L. Liu, L. P. Guo, J. X. Li, S. X. Pan, C. Q. Bian, L. Wang, X. Hu, X. J. Meng, L. H. Zhao, F. Deng, F. S. Xiao, *ChemSusChem*, 2017, **10**, 1186-1192.

31. B. Zou, L. Hao, L. Y. Fan, Z. M. Gao, S. L. Chen, H. Li, C. W. Hu, *J. Catal.*, 2015, **329**, 119-129.

32. S. Sahoo, D. Sarma, *Cryst. Growth Des.*, 2022, **22**, 5645-5657.

33. J. Tapiador, P. Leo, F. Gándara, G. Calleja, G. Orcajo, *J. CO_2 Util.*, 2022, **64**, 102166.

34. J. Tapiador, E. García-Rojas, P. Leo, C. Martos, G. Calleja, G. Orcajo, *Micropor. Mesopor. Mater.*, 2023, **361**, 112741.

35. J. Hutter, M. Iannuzzi, F. Schiffmann, J. VandeVondele, *WIRES Comput. Mol. Sci.*, 2014, **4**, 15-25.

36. J. P. Perdew, K. Burke, M. Ernzerhof, *Phys. Rev. Lett.*, 1996, **77**, 3865-3868.

37. J. VandeVondele, M. Krack, F. Mohamed, M. Parrinello, T. Chassaing, J. Hutter, *Comput. Phys. Commun.*, 2005, **167**, 103-128.

38. S. Goedecker, M. Teter, J. Hutter, *Phys. Rev. B: Condens. Matter*, 1996, **54**, 1703-1710.

39. C. Hartwigsen, S. Goedecker, J. Hutter, *Phys. Rev. B*, 1998, **58**, 3641-3662.

40. T. Lu, Q. Chen, *Comput. Theor. Chem.*, 2021, **1200**, 113249.